

RESEARCH

Open Access

An image formation algorithm for missile-borne circular-scanning SAR

Yesheng Gao^{*}, Kaizhi Wang and Xingzhao Liu

Abstract

Circular-scanning SAR is an imaging mode with its antenna beam rotating continuously with respect to the vertical axis. An image formation algorithm for the missile-borne circular-scanning SAR is proposed in this article. Based on the principle of the polar format algorithm, the focus algorithm is generalized to form each subimage when the antenna beam scans at an arbitrary position. By calculating the 2-D position of each calibration point between the scatterers and the subimages, a method is presented to correct the geometric distortion of each subimage. This method is able to correct the geometric distortion even in the case of high maneuvering. These subimages are then mosaicked together to form a circular image. The simulation results under three different maneuvering trajectories are given, the subimages are formed by the focusing algorithm, and then the final circular image can be formed by mosaicking 71 subimages, each of which is after geometric distortion correction. The simulations validate the proposed image formation algorithm, and the results satisfy system design requirements.

1 Introduction

Synthetic aperture radar (SAR) is a form of radar system to provide high resolution images with the use of the relative motion between the target region and the antenna, which is usually mounted on a moving platform [1-3]. The conventional platform includes aircraft, spacecraft, and satellite. The radar can also be mounted on a missile for military applications [4].

SAR system usually operates in three modes: stripmap, spotlight, and scan [1]. Circular-scanning SAR is different from these three modes, with its antenna beam rotating continuously with respect to the vertical axis [5,6]. It can provide SAR image of both sides of the flight path, and can also extend imaged area during a single pass with the same antenna. Missile-borne circular-scanning SAR suffers from complicated imaging problems: high speed, high squint angle, and high maneuvering. Sun discussed the properties of the circular-scanning SAR signal and presented an image formation algorithm based on the extended chirp scaling algorithm (ECSA) [5]. It is nature to increase the sampling rate and the memory storage for the ECSA as the squint angle increases. Li proposed a

geometric-distortion correction algorithm for the successive subimages formed by the linear range-Doppler algorithm (LRDA) [6]. LRDA is an efficient image formation algorithm, but it takes extra computations to compensate for motion errors due to the high maneuvering.

We concentrate on the image formation during the missile descending stage. An image formation algorithm for the missile-borne circular-scanning SAR is proposed. A processed aperture time is defined as the time during which the antenna beam rotates 360 degrees. The processed aperture is divided into many subapertures, the signal of which is processed by using the principle of the polar format algorithm (PFA) [1,2]. Each subaperture is used to form a SAR image, named *subimage*. The focus algorithm is generalized to form each subimage when the antenna beam scans at an arbitrary position. A geometric-distortion correction method is proposed. It corrects target locations by using 2-D interpolation in image domain. This method can work even in the case of high maneuvering. The successive subimages are mosaicked together to form a circular image. Compared with the existing algorithms of the circular-scanning SAR, the proposed algorithm does not need to increase the sampling rate and memory storage when the squint angle increases. Meanwhile, there is no extra computation to

*Correspondence: ysgao@sjtu.edu.cn

Department of Electronic Engineering, Shanghai Jiao Tong University, 800 Dongchuan Road, 200240, Shanghai, China

motion compensation since it is included in the subimage focusing algorithm.

The remainder of the article is organized as follows. In Section 2, the imaging geometry of the missile-borne circular-scanning SAR is introduced. In Section 3, the image formation algorithm is detailed. In Section 4, simulation results under three different maneuvering trajectories are described. Section 5 presents our conclusions.

2 Imaging geometry of the missile-borne circular-scanning SAR

The imaging geometry of missile-borne circular-scanning SAR is illustrated in Figure 1. Symbols are listed as follows. For clarity of the illustration, some symbols are not labeled in Figure 1.

- v_a : velocity of the missile. Its horizontal component coincides with the positive x -axis.
- H : altitude of the missile.
- θ_d : dive angle which identifies the direction of the missile velocity relative to the horizontal direction.
- p_m : the position of the antenna phase center (APC).
- p'_m : the corresponding nadir point of p_m .
- Ω : rotating speed of the antenna beam. It is considered positive when rotating counterclockwise.
- θ_r : the angle that goes counterclockwise from the positive x -axis to the ground beam orientation.
- ψ_a : incidence angle.
- β_r : two-way range beamwidth.
- β_a : two-way azimuth beamwidth.
- φ_g : projection of β_a onto the x - y plane.
- α : Doppler cone angle.
- θ_{gs} : ground squint angle.
- O_{temp} : temporary scene center. It coincides with the origin of the coordinate system when $t = 0$.

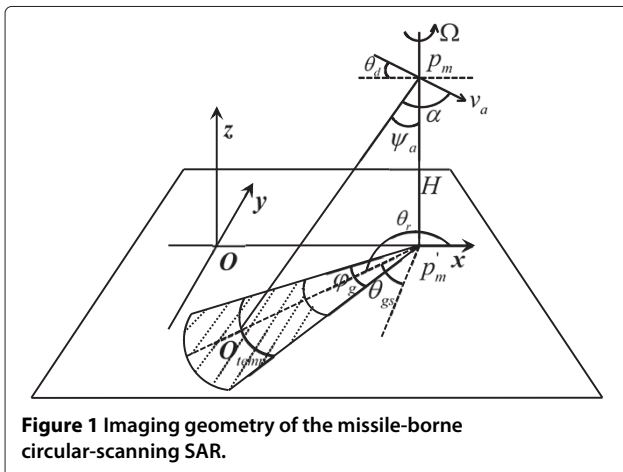


Figure 1 Imaging geometry of the missile-borne circular-scanning SAR.

θ_r changes with time and can be expressed as

$$\theta_r(t) = \theta_{r0} + \Omega \cdot t. \quad (1)$$

Here, assume that $\theta_{r0} = 180^\circ$, when $t = 0$.

According to the imaging geometry of the missile-borne circular-scanning SAR, φ_g can be expressed as

$$\varphi_g = 2 \cdot \arctan \left[\frac{\tan \left(\frac{\beta_a}{2} \right)}{\sin \psi_a} \right]. \quad (2)$$

Given the coordinate of $p_m [x(t), y(t), z(t)]$ at arbitrary time t , the size of the antenna footprint can be described as

$$\begin{cases} r_l(t) = z(t) \cdot \tan \left(\psi_a - \frac{\beta_r}{2} \right) \\ r_m(t) = z(t) \cdot \tan(\psi_a) \\ r_u(t) = z(t) \cdot \tan \left(\psi_a + \frac{\beta_r}{2} \right) \end{cases} \quad (3)$$

where $r_m(t)$ is the footprint radius (distance between p'_m and O_{temp}), $r_l(t)$ and $r_u(t)$ is the lower and upper limit radius, respectively.

Temporary scene center $O_{temp} ([x_{sc}(t), y_{sc}(t)])$ is calculated by

$$\begin{cases} x_{sc}(t) = x(t) + r_m(t) \cdot \cos \theta_r(t) \\ y_{sc}(t) = y(t) + r_m(t) \cdot \sin \theta_r(t) \end{cases} \quad (4)$$

In particular, $[x_{sc}(0), y_{sc}(0)] = [0, 0]$ according to the aforementioned assumption.

3 Image formation algorithm for the missile-borne circular-scanning SAR

The image formation algorithm for the missile-borne circular-scanning SAR is comprised of three steps: (1) subimage formation, (2) geometric-distortion correction, (3) image mosaicking. Subimages after correcting geometric distortion are mosaicked together to get the final circular image. These three steps are discussed in detail in the following sections.

3.1 Subimage formation

Define

$$\hat{t} = t - n \cdot T_{sub} \quad (n = 0, 1, \dots, N - 1) \quad (5)$$

where T_{sub} is the subaperture time, N is the total number of the subimages. In a single subaperture time ($-T_{sub}/2 \leq \hat{t} < T_{sub}/2$), the radar platform moves from the start of the subaperture to the end of the subaperture, θ_r changes from $\theta_r(t_n)$ to $\theta_r(t_n + T_{sub})$.

The overlap region of the two neighboring footprints is considered a spotlight imaging, the center angle of

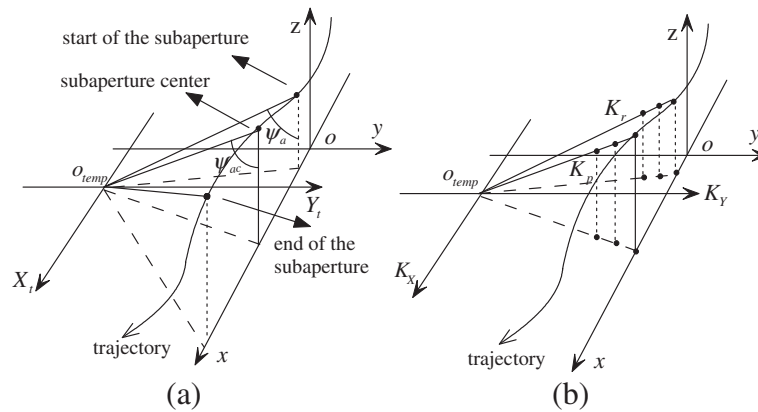


Figure 2 Data collection model under high maneuvering. **(a)** data collection in spatial domain; **(b)** data collection in wavenumber domain.

the sector $\Delta\theta_r$ can be approximated as $\Delta\theta_r \approx \theta_r(t_n + T_{sub}) - \theta_r(t_n)$. The lower limit of $\Delta\theta_r$ is determined by the required cross-range resolution of the subimages [6].

The subimage focus algorithm is generalized to process each subaperture data when the antenna beam scans at an arbitrary position, it is based on the principle of the Polar format algorithm (PFA). PFA is a typical spotlight SAR imaging algorithm [1,2,7]. It can achieve 3-D motion compensation, and the motion compensation is carried out without any extra computations [1,8]. The data collection surface (DCS) is determined by the trajectory and the scene center. When the missile is highly maneuvering, the DCS is shown in Figure 2. ψ_a is the incidence angle, and ψ_{ac} is its value when $\hat{t} = 0$.

In the subimage formation, x - y plane is selected as the focus target plane (FTP) and the image display plane (IDP). The signal in the DCS can be projected onto this plane. With reference to Figure 2b, the signal coordinate in the DCS can be expressed as (in wavenumber domain)

$$K_r = \frac{4\pi}{c} \cdot f \quad (6)$$

where f is the signal frequency, c is the velocity of light. By multiplying the sine of the incidence angle $\sin \psi_a$, Equation (6) can be projected onto the FTP with

$$K_p = K_r \cdot \sin \psi_a = \frac{4\pi}{c} \cdot f \cdot \sin \psi_a. \quad (7)$$

The effect of maneuvering motion on the data projection is illustrated in Figure 3. When the platform trajectory is ideal (horizontal, linear, constant velocity), the signal projection is placed as shown in Figure 3a. While the missile is highly maneuvering, the same sample of each pulse is projected to different positions along the radial line in the FTP, as shown in Figure 3b.

Line-of-sight polar interpolation (LOSPI) is applied to the projected data. With LOSPI, the image display coordinates correspond to the range and cross-range coordinates in target space. Different θ_r changes the range and cross-range direction in target space and causes the orientation of the imaged scene to rotate with respect to image display coordinates. Then range and cross-range IFFT are used to obtain the subimages. The flowchart of the subimage formation is illustrated in Figure 4. This focus

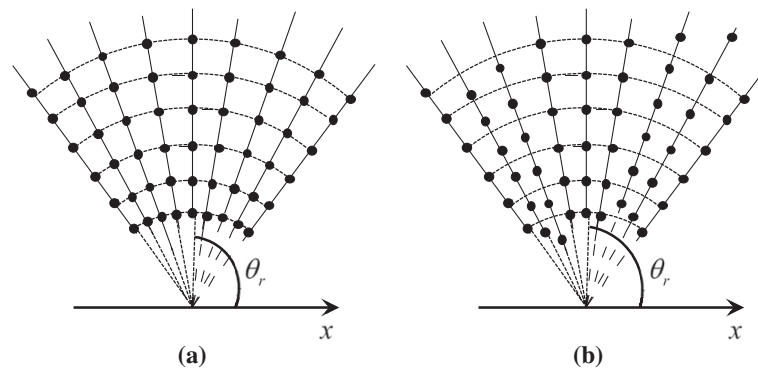
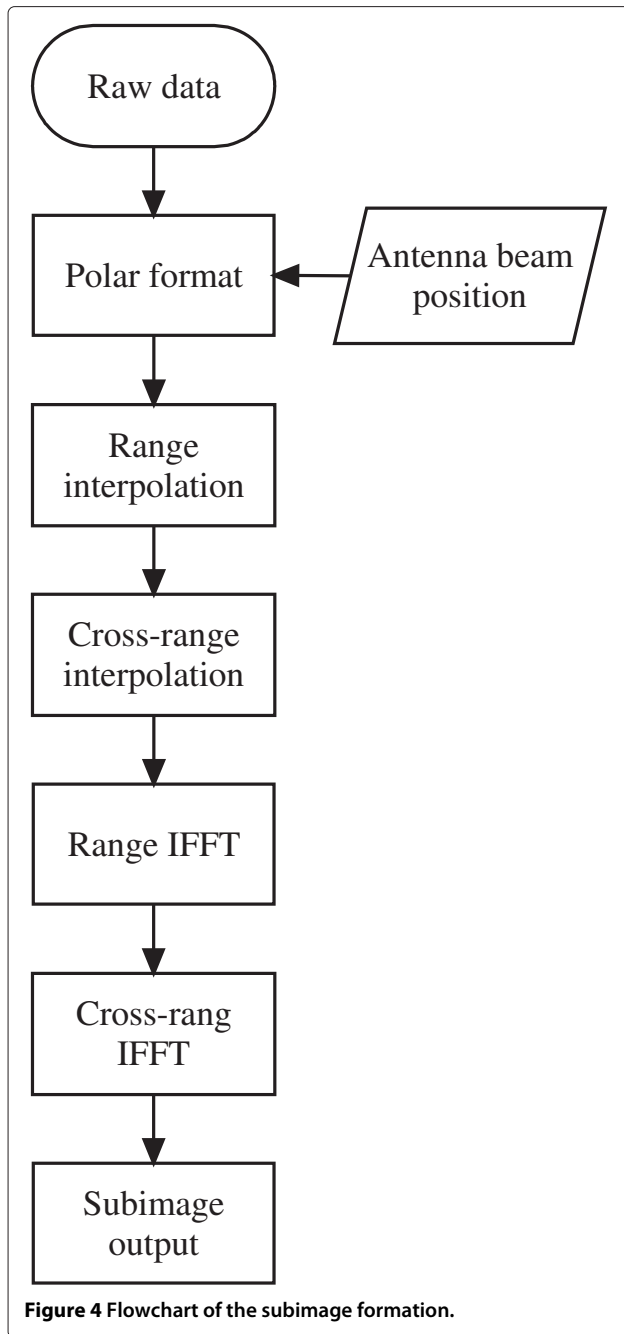


Figure 3 The effect of maneuvering motion on the data projection. **(a)** data projection of ideal trajectory; **(b)** data projection of maneuvering motion.



algorithm is based on the principle of the PFA, it is generalized to focus each subimage when the antenna beam scans at an arbitrary position. The resulting subimages suffer from the geometric distortion [1]. The geometric distortion is harmful to the image mosaicking.

3.2 Geometric-distortion correction

The geometric distortion is inevitable, its effects become more evident as the resolution and the squint angle increase [9]. It is necessary to correct geometric distortion

before imaging mosaicking. Because the geometric distortion is spatial-variant, its correction must be implemented by calculating the 2-D position of each calibration point between the scatterers and the subimages [6].

The model for the geometric-distortion correction is demonstrated in Figure 5. The calibration grid is in x - y plane and parallel to the x - and y -axes. The intervals of two adjacent calibration points are $\Delta x = p_x$ and $\Delta y = p_y$, with p_x and p_y denoting the range and azimuth pixel resolution, respectively. The x_t - y_t coordinate system is established as shown in Figure 5, with its origin locating at the temporary scene center O_{temp} . The y_t -axis indicates the ground beam orientation. Given the coordinate (x, y) in the x - y coordinate system, its corresponding coordinate (x_t, y_t) in the x_t - y_t coordinate system can be expressed as

$$\begin{cases} x_t = -(x - x_{sc}) \cdot \sin \theta_a + (y - y_{sc}) \cdot \cos \theta_a \\ y_t = -(x - x_{sc}) \cdot \cos \theta_a - (y - y_{sc}) \cdot \sin \theta_a \end{cases} \quad (8)$$

where θ_a is the angle that goes counterclockwise from the X_t -axis to the y_t -axis. The X_t - Y_t - Z_t coordinate system is established for derivation convenience, as shown in Figure 6. The X_t -axis is perpendicular to the y -axis, the Y_t -axis is perpendicular to the x -axis, Z_t -axis follows the right-hand rule, the origin locates at O_{temp} .

In this section, we derive the position calculation of a calibration point between the scatterer and the subimage. The derivation is in a general form and is even suited for the case of high maneuvering. Let $[f_x(t), f_y(t), f_z(t)]$ be the APC position in the x - y - z coordinate system. $[f_x(t), f_y(t), f_z(t)]$ can be transformed into the X_t - Y_t - Z_t coordinate system by

$$\begin{cases} F_X(t) = x_{sc} - f_x(t) \\ F_Y(t) = y_{sc} - f_y(t) \\ F_Z(t) = f_z(t) \end{cases} \quad (9)$$

The data coordinate in the wavenumber domain is illustrated in Figure 7. (x_p, y_p) is the coordinate of the received data in the wavenumber domain, it can be expressed as

$$\begin{cases} x_p = -K \cdot \sin(\theta_a - \theta_{ac}) \\ y_p = K \cdot \cos(\theta_a - \theta_{ac}) - K_c \end{cases} \quad (10)$$

where

$$K_c = \frac{4\pi \sin \psi_{ac}}{c} f_c, \quad (11)$$

and

$$K = K_c \frac{\sin \psi_a}{\sin \psi_{ac}} \cdot f_c \left[f_c + k \left(\tau - \frac{2R_a}{c} \right) \right]. \quad (12)$$

k is the chirp rate of the transmitted signal, f_c is the carrier frequency, τ represents fast time.

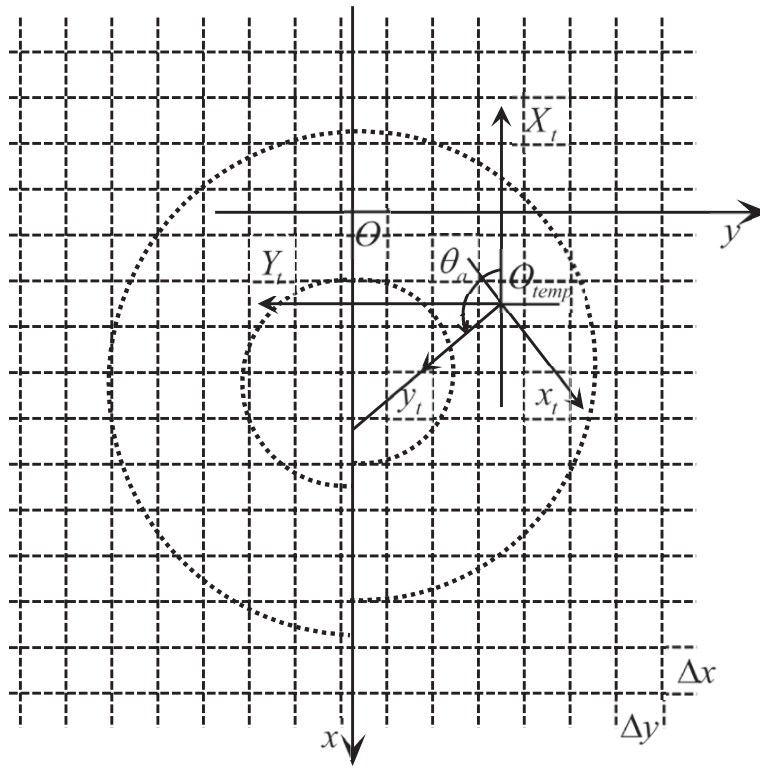


Figure 5 Model for the geometric-distortion correction.

Assume that a calibration point locating at (T_X, T_Y, T_Z) in the X_t - Y_t - Z_t coordinate system, the differential range is

$$\begin{aligned}
 R_{\Delta} &= R_t - R_a \\
 &= \sqrt{[F_X(t) - T_X]^2 + [F_Y(t) - T_Y]^2 + [F_Z(t) - T_Z]^2} \\
 &\quad - \sqrt{F_X^2(t) + F_Y^2(t) + F_Z^2(t)},
 \end{aligned}
 \tag{13}$$

and the sine of the incidence angle can be expressed as

$$\sin \psi_a = \frac{\sqrt{F_X^2(t) + F_Y^2(t)}}{R_a}
 \tag{14}$$

where R_t is the distance from the APC to the calibration point, R_a is the distance from the APC to the temporary scene center.

After removing the residual video phase (RVP), the phase of the echo is expressed as

$$\Phi = -K \cdot \frac{R_{\Delta}}{\sin \psi_a}.
 \tag{15}$$

Using Equations (10) and (15), the Taylor series expansion of the phase $\Phi(x_p, y_p)$ about $(x_p, y_p) = (0, 0)$ is

$$\begin{aligned}
 \Phi(x_p, y_p) &= a_0 + a_1 \cdot x_p + a_2 \cdot y_p + a_{11} \cdot x_p^2 + a_{12} \cdot x_p \cdot y_p \\
 &\quad + a_{22} \cdot y_p^2 + \dots
 \end{aligned}
 \tag{16}$$

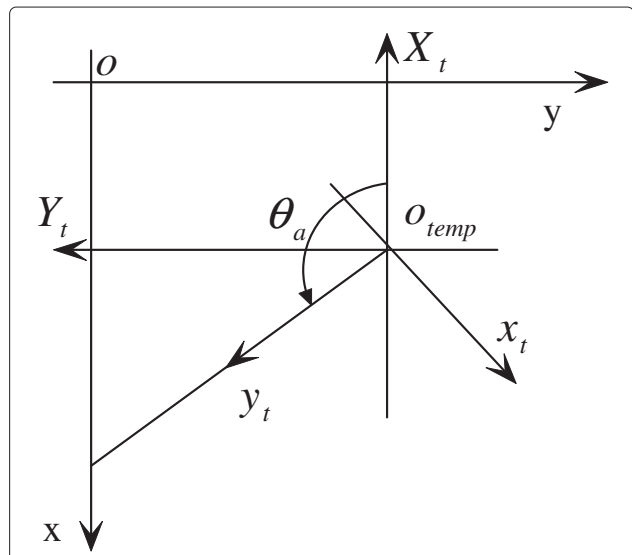
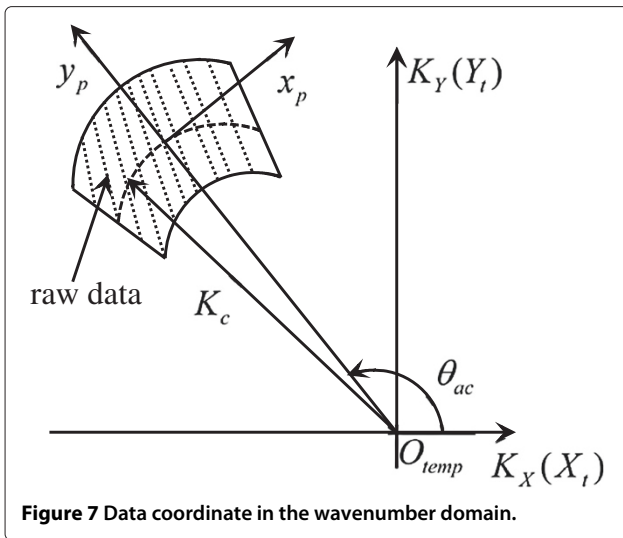


Figure 6 Coordinate transformation.



Here, the higher order terms are not emphasized. According to the full differential formula, a_1 and a_2 have the forms as follows

$$\begin{cases} a_1 = \left. \frac{\partial \Phi}{\partial x_p} \right|_c = \left(\frac{\partial \Phi}{\partial K} \frac{\partial K}{\partial x_p} + \frac{\partial \Phi}{\partial \theta_a} \frac{\partial \theta_a}{\partial x_p} \right) \Big|_c = -\frac{1}{K_c} \frac{\partial \Phi}{\partial \theta_a} \Big|_c \\ a_2 = \left. \frac{\partial \Phi}{\partial y_p} \right|_c = \left(\frac{\partial \Phi}{\partial K} \frac{\partial K}{\partial y_p} + \frac{\partial \Phi}{\partial \theta_a} \frac{\partial \theta_a}{\partial y_p} \right) \Big|_c = \frac{\partial \Phi}{\partial K} \Big|_c \end{cases} \quad (17)$$

Equation (17) can be further written as

$$\begin{cases} a_1 = -\frac{1}{K_c} \cdot \left. \frac{dt}{d\theta_a} \right|_c \cdot \left. \frac{\partial \Phi}{\partial t} \right|_c = \left. \frac{dt}{d\theta_a} \right|_c \cdot \left(\frac{R_{\Delta}}{\sin \psi_a} \right)' \Big|_c \\ a_2 = -\frac{R_{\Delta c}}{\sin \psi_{ac}} \end{cases} \quad (18)$$

$\left. \frac{dt}{d\theta_a} \right|_c$ and $\left(\frac{R_{\Delta}}{\sin \psi_a} \right)' \Big|_c$ in Equation (18) can be calculated as follows.

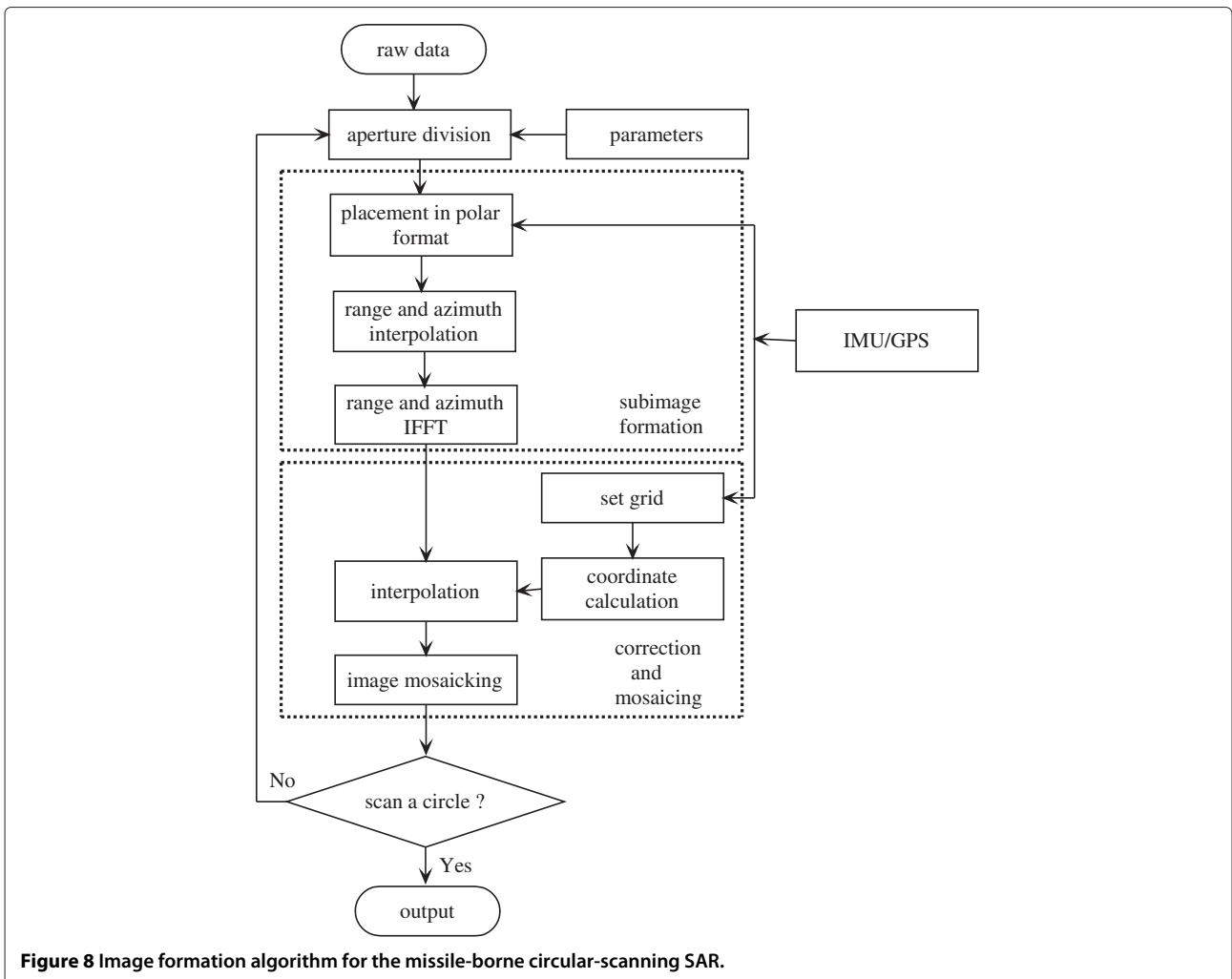


Table 1 Simulation parameters

Parameter	Value
Horizontal velocity v_x	956 m/s
Platform altitude H	> 10 km
Antenna rotating speed Ω	293 °/s
Dive angle θ_d	45.5 °/s
Bandwidth B	32 MHz
Range beamwidth β_r	21 °
Azimuth beamwidth β_a	3.9 °
Sector center angle $\Delta\theta_r$	10 °
Scene extent $W_x \times W_y$	20 km \times 20 km
Pixel resolution $p_r \times p_a$	10 m \times 10 m

Using $\cot \theta_a = \frac{F_X(t)}{F_Y(t)}$, we can obtain

$$-\frac{1}{\sin^2 \theta_a} d\theta_a = \frac{F'_X(t)F_Y(t) - F_X(t)F'_Y(t)}{F_Y^2(t)} dt. \quad (19)$$

Thus,

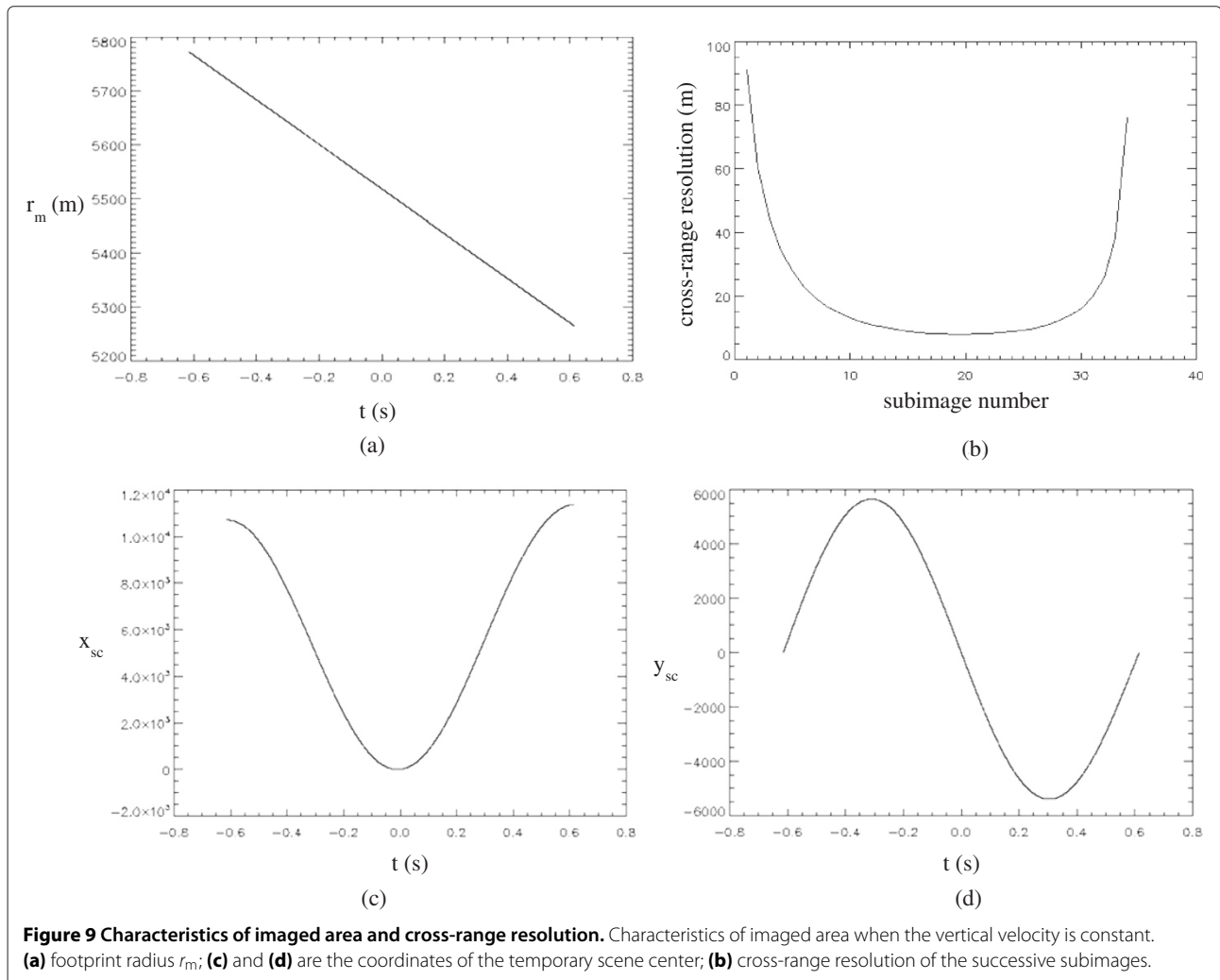
$$\begin{aligned} \left. \frac{dt}{d\theta_a} \right|_c &= -\frac{F_Y^2(t)}{F'_X(t)F_Y(t) - F_X(t)F'_Y(t)} \cdot \frac{1}{\sin^2 \theta_a} \Big|_c \\ &= -\frac{F_{Yc}}{V_{Xc} - V_{Yc} \cot \theta_{ac}} \cdot \frac{1}{\sin^2 \theta_{ac}} \\ &= -\frac{F_{Yc} / \sin \theta_{ac}}{V_{Xc} \sin \theta_{ac} - V_{Yc} \cos \theta_{ac}}, \end{aligned} \quad (20)$$

and

$$\left(\frac{R_{\Delta}}{\sin \psi_a} \right)' \Big|_c = \frac{R'_{\Delta c} \sin \psi_{ac} - R_{\Delta c} \sin' \psi_{ac}}{\sin^2 \psi_{ac}} \quad (21)$$

where

$$\begin{aligned} R'_{\Delta c} &= \frac{(F_{Xc} - T_X) \cdot F'_{Xc} + (F_{Yc} - T_Y) \cdot F'_{Yc} + (F_{Zc} - T_Z) \cdot F'_{Zc}}{\sqrt{(F_{Xc} - T_X)^2 + (F_{Yc} - T_Y)^2 + (F_{Zc} - T_Z)^2}} \\ &= \frac{F_{Xc}F'_{Xc} + F_{Yc}F'_{Yc} + F_{Zc}F'_{Zc}}{\sqrt{F_{Xc}^2 + F_{Yc}^2 + F_{Zc}^2}} \end{aligned}$$



$$\begin{aligned}
 &= \frac{\vec{R}_{tc} \cdot \vec{V}_{ac}}{R_{tc}} - \frac{\vec{R}_{ac} \cdot \vec{V}_{ac}}{R_{ac}} = \frac{(\vec{R}_{ac} - \vec{r}_t) \cdot \vec{V}_{ac}}{R_{tc}} - \frac{\vec{R}_{ac} \cdot \vec{V}_{ac}}{R_{ac}} \\
 &= -\frac{\vec{r}_t \cdot \vec{V}_{ac}}{R_{tc}} - \frac{R_{\Delta c} \cdot (\vec{R}_{ac} \cdot \vec{V}_{ac})}{R_{tc} \cdot R_{ac}},
 \end{aligned} \tag{22}$$

and

$$\begin{aligned}
 \sin' \psi_{ac} &= \frac{\frac{F_{Xc}F'_{Xc} + F_{Yc}F'_{Yc}}{\sqrt{F_{Xc}^2 + F_{Yc}^2}} R_{ac} - \frac{\vec{R}_{ac} \cdot \vec{V}_{ac}}{R_{ac}} \sqrt{F_{Xc}^2 + F_{Yc}^2}}{R_{ac}^2} \\
 &= \frac{V_{Xc} \cos \theta_{ac} + V_{Yc} \sin \theta_{ac}}{R_{ac}} - \frac{\sin \psi_{ac}}{R_{ac}} \frac{\vec{R}_{ac} \cdot \vec{V}_{ac}}{R_{ac}}.
 \end{aligned} \tag{23}$$

Here, \vec{R}_t is the APC position vector relative to the calibration point, \vec{R}_a is the APC position vector relative to the temporary scene center, \vec{r}_t is the calibration point position vector relative to the temporary scene center. \vec{V}_{ac} is the velocity vector in the X_t - Y_t - Z_t coordinate system, V_{Xc} and

V_{Yc} are its components in the X_t - and Y_t -axes. The subscript c refers to the values of the corresponding variables at the subaperture center.

The position of a calibration point in the corresponding subimage is derived. Given a calibration point locating at (x, y) in the x - y coordinate system (a flat earth is assumed), its corresponding position in the subimage can be obtained by

$$\begin{cases} N_a = -\frac{a_1}{p_a} + \frac{N_{a\text{FFT}}}{2} \\ N_r = -\frac{a_2}{p_r} + \frac{N_{r\text{FFT}}}{2} \end{cases} \tag{24}$$

where $p_r = \frac{c}{2B_r} \frac{N_{r\text{out}}}{N_{r\text{FFT}}}$, $p_a = \frac{c}{2B_a} \frac{N_{a\text{out}}}{N_{a\text{FFT}}}$. B_r and B_a are range and azimuth output bandwidth, $N_{x\text{out}}$ is the sample number of the interpolation output in the range/azimuth direction, $N_{x\text{FFT}}$ is the FFT size.

Specially, we present the form of equation (18) under vertical maneuvering. That is, only the vertical component of v_a is changing with time, its horizontal component is a constant. This is due to the fact that the impact of the

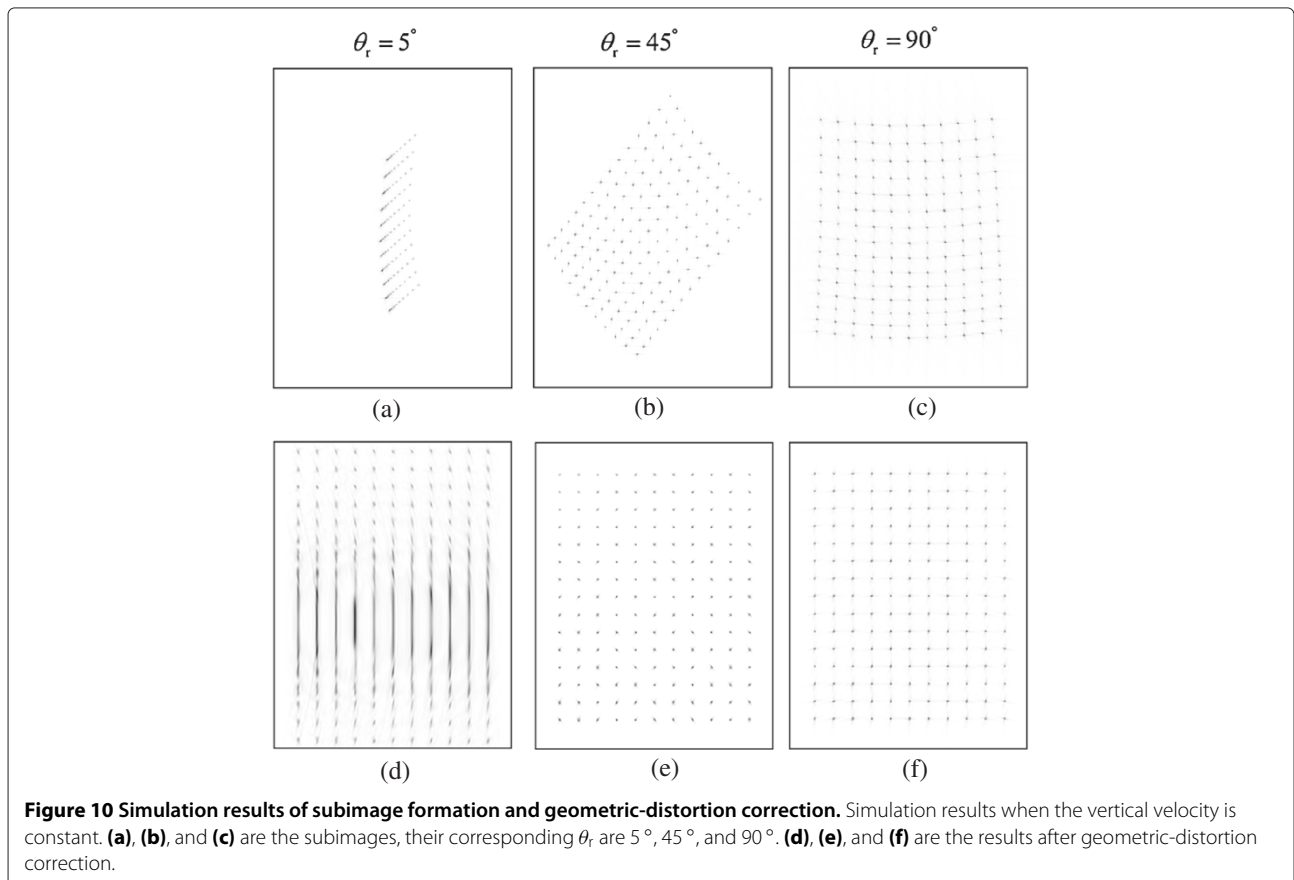
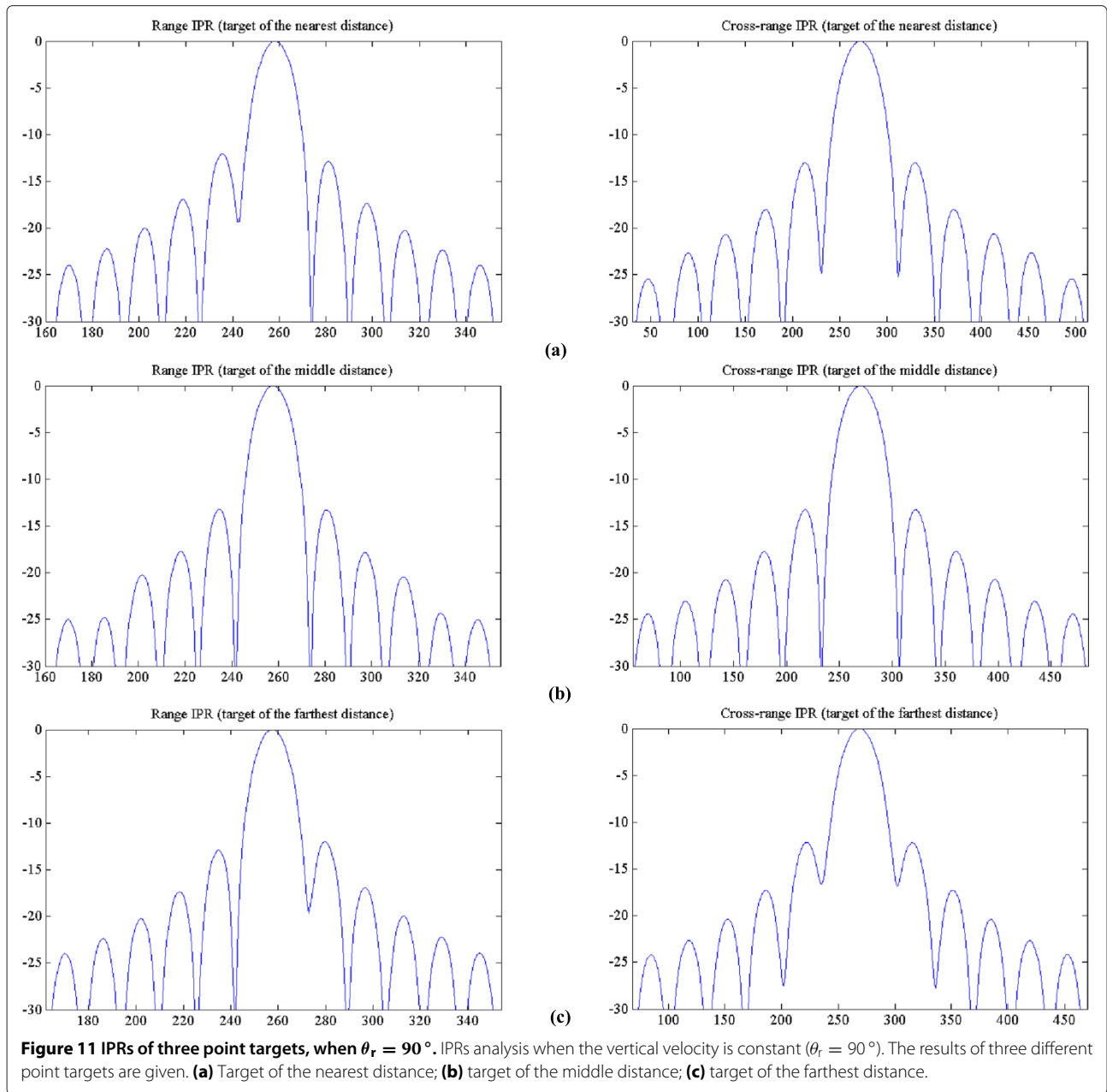


Figure 10 Simulation results of subimage formation and geometric-distortion correction. Simulation results when the vertical velocity is constant. **(a)**, **(b)**, and **(c)** are the subimages, their corresponding θ , are 5° , 45° , and 90° . **(d)**, **(e)**, and **(f)** are the results after geometric-distortion correction.



vertical maneuvering is serious to the circular-scanning SAR, and the vertical maneuvering is used in the following simulation experiments.

$$\begin{aligned}
 a_1 = x_p - \frac{1}{2R_{ac} \cdot \sin \theta_{ac} \cdot \sin \psi_{ac}} & \left\{ \cos \theta_{ac} \cdot \sin^2 \psi_{ac} \cdot y_p^2 \right. \\
 & \times [1 + 2 \sin^2 \psi_{ac}] - 2 \sin^2 \psi_{ac} \cdot T_X \cdot y_p - \cos \theta_{ac} \cdot r_t^2 \left. \right\} \\
 & - \frac{V_{Zc} \cdot \sin^2 \psi_{ac} \cdot \cos \psi_{ac}}{R_{ac} \cdot V_{Xc} \cdot \sin \theta_{ac}} \cdot y_p^2,
 \end{aligned} \tag{25}$$

and

$$a_2 = y_p - \frac{1}{2R_{ac} \cdot \sin \psi_{ac}} \left(r_t^2 - \sin^2 \psi_{ac} \cdot y_p^2 \right). \tag{26}$$

Here, R_a is the distance between the APC and the temporary scene center. r_t is the distance between the

Table 2 PSLRs analysis of the IPRs (vertical velocity is constant)

	PSLR of range IPR	PSLR of cross-range IPR
Nearest target	-12.04 dB	-13.03 dB
Middle target	-13.28 dB	-13.23 dB
Farthest target	-12.14 dB	-12.01 dB

temporary scene center and the calibration point. T_X is the coordinate of the calibration point in the X_t -axis, V_Z is the component of v_a in the Z_t -axis, V_X in the X_t -axis, these variables are evaluated in the X_t - Y_t coordinate system. θ_{ac} , ψ_{ac} , V_{xc} , V_{zc} , and R_{ac} are the values of the corresponding variables at the subaperture center.

The geometric distortion can be corrected as follows.

Step 1: Set calibration grid, as shown in Figure 5.

Step 2: Calculate the position of each calibration point in the subimage, (N_r, N_a) . These calibration points are constrained within the instantaneous imaging area.

Step 3: Obtain the intensity of the corresponding position via 2-D interpolation.

3.3 Image mosaicking

Subimages are focused as discussed in Section 3.1. The method proposed in Section 3.2 can correct their geo-

metric distortion. The final circular image is formed by mosaicking together these subimages. The image mosaicking can be described as follows.

Step 1: Calculate the size of the final output image, allocate a matrix to store the image. The complete illuminated area ($0^\circ \leq \theta_r < 360^\circ$) can be calculated according to the radar system parameters. Thus, the size of the output image can be determined when p_r and p_a are known. It should be noted that each pixel in the output image corresponds to a calibration point.

Step 2: Correct the geometric distortion of each calibration point in the temporary illuminated area. The temporary illuminated area can be calculated using the radar system parameters, the instantaneous radar platform position and the value of θ_r . The geometric distortion of each calibration point in this area can be corrected by using the method described

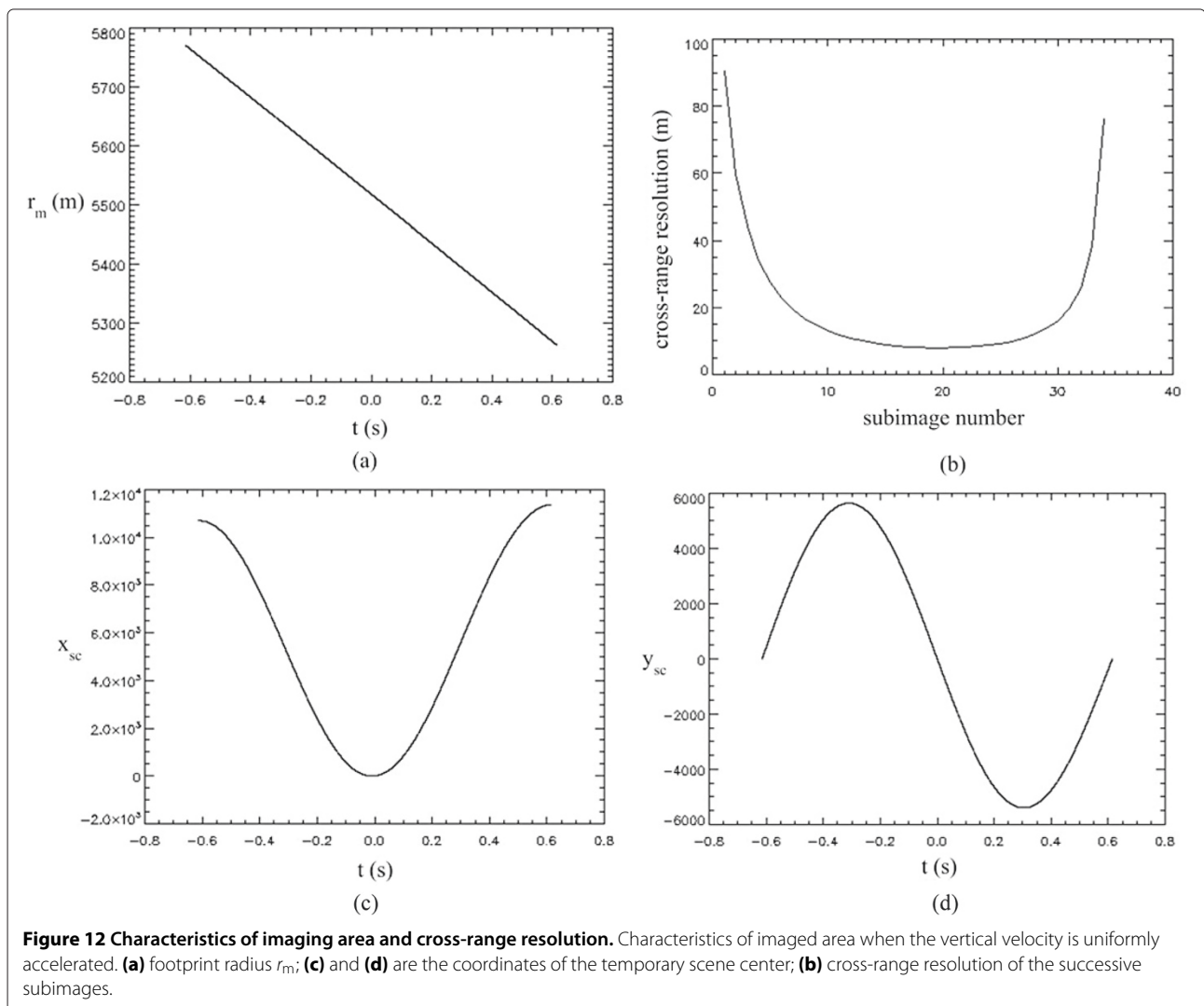


Figure 12 Characteristics of imaging area and cross-range resolution. Characteristics of imaged area when the vertical velocity is uniformly accelerated. (a) footprint radius r_m ; (c) and (d) are the coordinates of the temporary scene center; (b) cross-range resolution of the successive subimages.

in Section 3.2. Then the subimage without geometric distortion is stored into the positions where the calibration points are located.

Step 3: If all the subimages are formed (in the later simulations, the number of subimages to constitute a circular image is 71), output the final circular image. Otherwise, return to Step 2 to form the next subimage. Thus, the final circular image can be formed by adding successive subimages.

The geometric distortion is corrected point-by-point, the successive subimages are mosaicked together to form the final circular image. This can well describe the circular-scanning SAR imaging procedure. Note that not only the final circular image can be formed, but the image with the beam rotating at an arbitrary position can be produced. The final image product and the intermediate result are stored in the same matrix, which reduces the memory requirement and computational complexity. The image formation algorithm for the missile-borne circular-scanning SAR is demonstrated in Figure 8.

3.4 Computational consideration

The image formation algorithm of the missile-borne circular-scanning SAR is detailed in the three preceding sections. This algorithm is comprised of three steps: subimage formation, geometric-distortion correction, and image mosaicking. In the subimage formation, the major computational burden is the interpolation and the IFFT operation. The computational complexity of the interpolation operation can be expressed as

$$CP = 0.4 \cdot L_{out} [(L_f - 1) r_{DS} + 1] M_k \quad (27)$$

where L_{out} is the output length of the interpolation, L_f is the length of the filter, r_{DS} is the downsampling ratio, M_k is a constant and its typical value is 1.25 [1]. The interpolation can also be implemented by chirp z-transform [9]. The lengths of IFFT operation are N_{rout} and N_{aout} in the range and cross-range direction, respectively. After position calculation, the geometric-distortion correction is implemented by interpolation operation, the computational complexity can be determined by Equation (27).

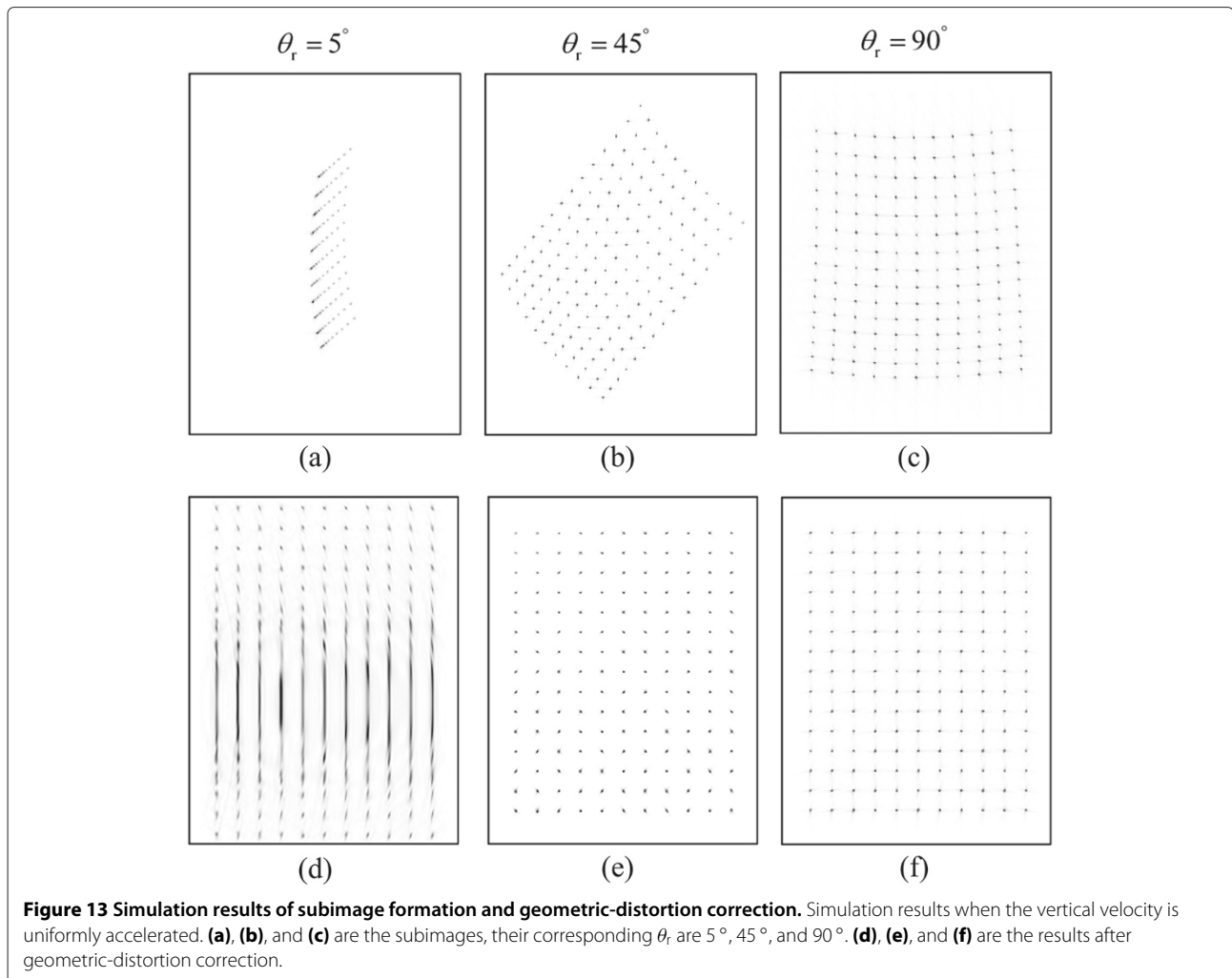


Figure 13 Simulation results of subimage formation and geometric-distortion correction. Simulation results when the vertical velocity is uniformly accelerated. (a), (b), and (c) are the subimages, their corresponding θ_r are 5° , 45° , and 90° . (d), (e), and (f) are the results after geometric-distortion correction.

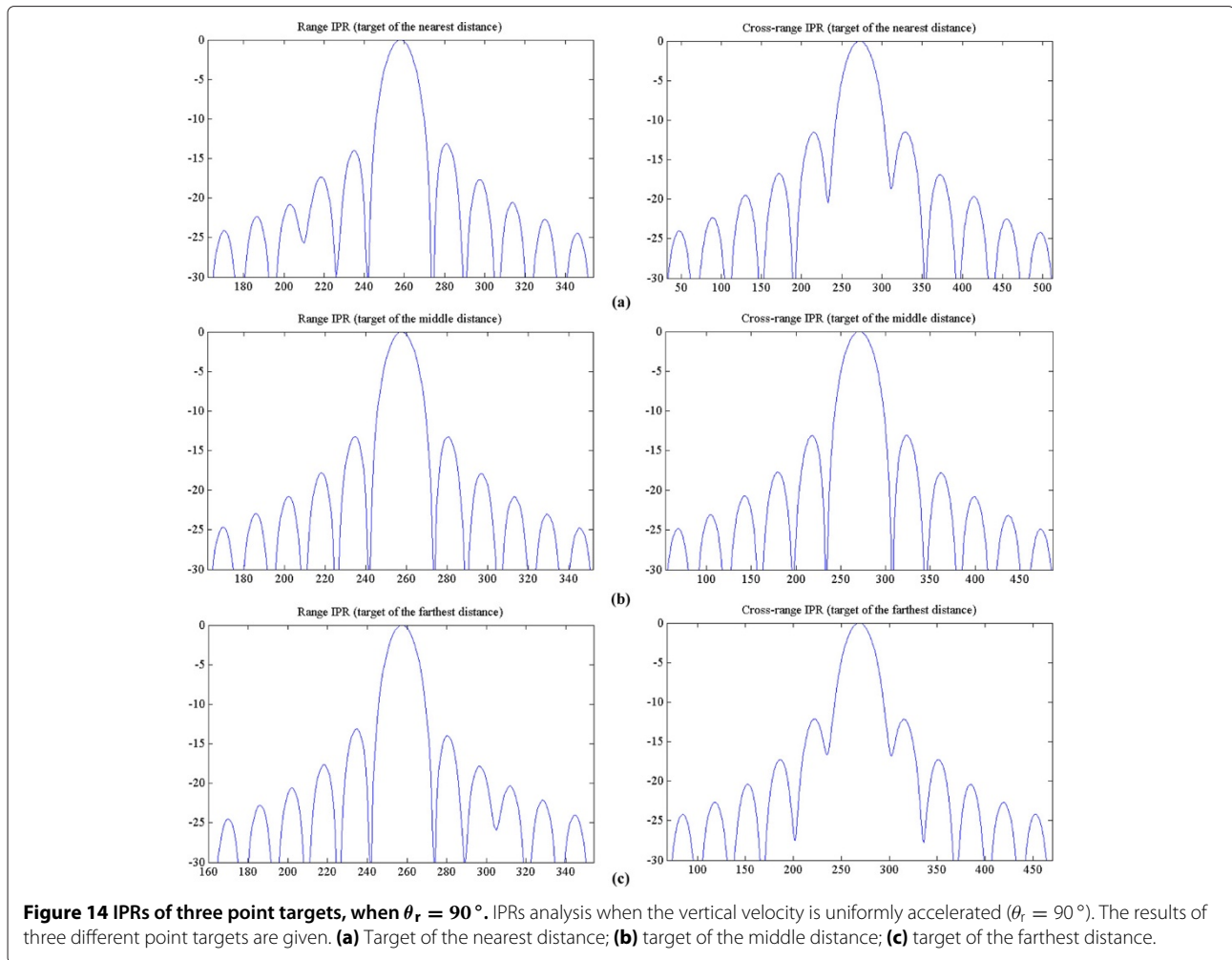


Image mosaicking is separated as the third step, but its realization is included in geometric-distortion correction and no extra computation is needed.

4 Simulation results

To validate the performance of the proposed algorithm, simulation results under three different maneuvering motions are presented. The primary parameters of a Ku-band radar system are given in [6] and are listed in Table 1.

In Section 4.1, the vertical velocity v_z does not change with time, and the horizontal velocity v_x is also constant. To validate the image formation algorithm in subimage formation and geometric-distortion correction, the simulated point targets are placed as a rectangle with the size of 11×15 , the distance between two adjacent targets is 200 m. The characteristics of the imaged area (footprint radius, and coordinates of the temporary scene center) and the cross-range resolution of successive subimages are analyzed. Three subimages and their geometric-distortion correction results are given. Quantitative analysis of the result is also given.

In Section 4.2, the horizontal velocity is still constant, the vertical velocity is uniformly accelerated. The point targets are placed the same as those in Section 4.1. The characteristics of imaged area, the cross-range resolution of successive subimages, and three typical subimages are given. Quantitative analysis of the result is also given.

In Section 4.3, the horizontal velocity is still constant, the vertical velocity changes with time in sinusoidal form. In this section, the final circular image is give. The ground point targets are placed uniformly with the interval of $200 \text{ m} \times 200 \text{ m}$, the total number of the targets is 95×95 . The cross-range resolution of successive subimages are illustrated.

Table 3 PSLRs analysis of the IPRs (vertical velocity is uniformly accelerated)

	PSLR of range IPR	PSLR of cross-range IPR
Nearest target	-13.11 dB	-11.54 dB
Middle target	-13.25 dB	-13.13 dB
Farthest target	-13.19 dB	-12.00 dB

The major computations involved in the image formation algorithm are interpolation and IFFT, both operations are applied in the range and azimuth directions. In the range direction, the value of L_{out} is 2048, L_f is 8, r_{DS} is 1. In the azimuth direction, L_{out} is 340, L_f is 8, r_{DS} is 1.51. The IFFT size in range is 2048, azimuth 512.

4.1 Constant velocity in the vertical direction

Vertical velocity v_z is set at -973 m/s. The footprint radius is shown in Figure 9a, its value decreases gradually due to the platform altitude reduction. The coordinate of the temporary scene center is illustrated in Figure 9c,d, respectively. Figure 9b shows the cross-range resolution ($0^\circ \leq \theta_r \leq 180^\circ$). The resolution decreases as the squint angle increases, the finest resolution can be achieved when $\theta_r = 90^\circ$ or $\theta_r = 270^\circ$.

The subimages of three typical values of θ_r are shown in Figure 10. Figure 10a–c are the subimages when $\theta_r = 5^\circ$,

45° , and 90° . The geometric distortion is evident in these subimages, especially in Figure 10a,b. Because LOSPI is applied, the received data at different look angles change the range and cross-range directions in target space. The orientation of the resultant subimage rotates with respect to the image display coordinates. Figure 10d–f are the geometric-distortion correction results. Although the geometric distortion is corrected, it is also difficult to distinguish targets in cross-range direction in Figure 10d since θ_r is around 0° . It is the inevitable drawback of side-look SAR to distinguish targets at the forward and backward directions [1].

The impulse responses (IPRs) of three point targets at different distances are given in Figure 11. The three targets locate at the nearest, middle, and farthest distances from the APC. With reference to Figure 11, the peak side-lobe ratio (PSLRs) of range IPRs and cross-range IPRs are analyzed, as given in Table 2 (no windowing functions are

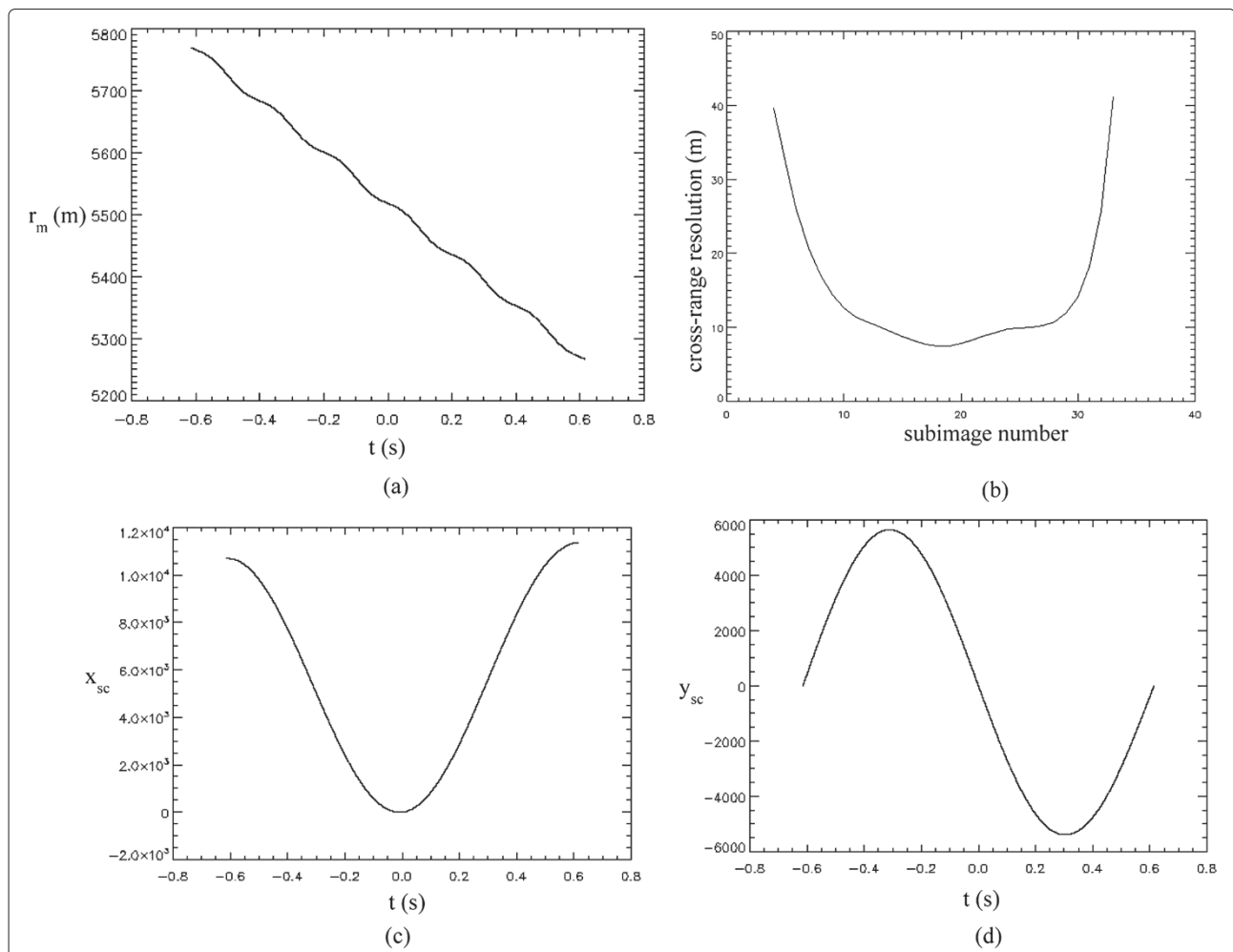


Figure 15 Characteristics of imaging area and cross-range resolution. Characteristics of imaged area when the vertical velocity changes in sinusoidal form. (a) Footprint radius r_m ; (c) and (d) are the coordinates of the temporary scene center; (b) cross-range resolution of the successive subimages.

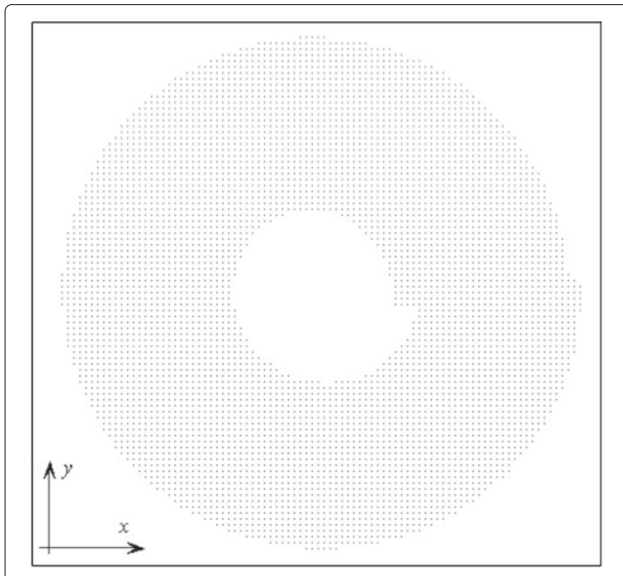


Figure 16 Locations of the illuminated point targets.

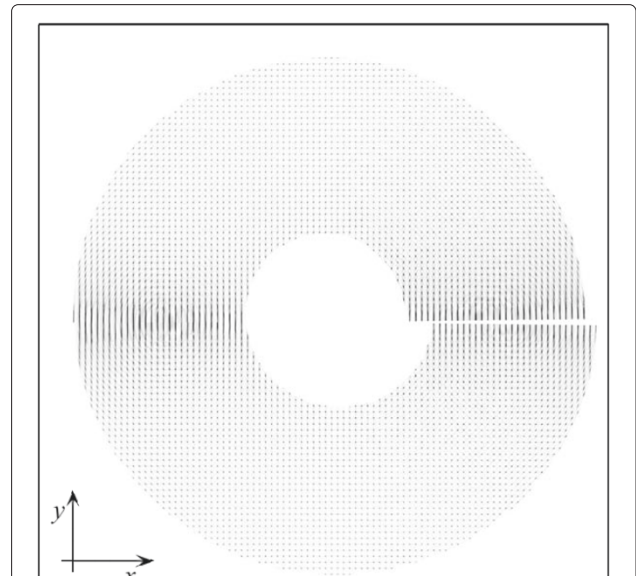


Figure 17 Imaging result of missile-borne circular-scanning SAR.

used). The point targets located in these three different distances are well focused.

4.2 Uniformly acceleration in the vertical direction

The vertical velocity is set in the form of $v_z = v_{z0} + a_z t$, with $v_{z0} = -973$ m/s and $a_z = -10$ m/s². When θ_r rotates from 0° to 360° , the change of the footprint radius r_m is illustrated in Figure 12a. The cross-range resolution of successive subimages are shown in Figure 12b, only the part with θ_r changing from 0° to 180° is shown due to the symmetry. The coordinates of temporary scene center as shown in Figure 12c,d correspond with θ_r , they can indicate the imaged area.

Three subimages and their corresponding geometric-distortion correction results are shown in Figure 13. Figure 13a–c are the subimages when $\theta_r = 5^\circ, 45^\circ$, and 90° , the results of geometric-distortion correction are illustrated in Figure 13d–f. The geometric distortion in the subimages is obvious. These image products do not meet the application and mosaicking requirements. The geometric distortion is then corrected and the positions of the point targets are identical to their assumed positions. The simulation results show that the proposed image formation algorithm can form subimages without geometric distortion even under the high maneuvering motions.

The impulse responses (IPRs) of three point targets at different distances are given in Figure 14. With reference to Figure 14, the peak sidelobe ratio (PSLR)s of range IPRs and cross-range IPRs are analyzed, as given in Table 3 (no windowing functions are used). The IPRs analysis demonstrates that the targets located in the whole illuminated area can be well focused, and the performance meets the system requirement.

4.3 Vertical velocity changes with time in sinusoidal form

In the 3rd condition, vertical velocity has the form of $v_z = v_{z0} + 2\pi \cdot f_z \cdot A_z \cdot \cos(2\pi f_z t)$, where $v_{z0} = -973$ m/s, $f_z = 5$ Hz, $A_z = 15$ m. The trajectory perturbation in vertical direction is studied in this simulation, and the motion parameters are set according to [10]. The footprint radius decreases as the platform altitude decreases, as shown in Figure 15a. Different subimages have different cross-range resolution, as shown in Figure 15b, the minimum value is about 10 m. The antenna beam pointing changes with θ_r , the coordinates of temporary scene center are illustrated in Figure 15c,d.

With θ_r rotating from 0° to 360° , the locations of the illuminated point targets are illustrated in Figure 16. The annular shape is determined by the radar system and the platform motion. The imaging result of the missile-borne circular-scanning SAR is shown in Figure 17. The complete circular image is obtained by mosaicking 71 successive subimages. In Figure 17, the point targets are uniformly distributed, their positions are identical to those shown in Figure 16. It is interesting that the targets locating at the forward and backward directions cannot be distinguished. It is due to the fact that the contour lines of the iso-range and iso-Doppler circles are nominally parallel in these two directions, suggesting that the inability of range-Doppler discrimination to position ground echoes.

5 Conclusion

An image formation algorithm for the missile-borne circular-scanning SAR is proposed in this article. The final circular image is formed through subimage formation, geometric-distortion correction, and image mosaicking.

Simulation results under three different maneuvering motions are given, each point target in the illuminated area is well focused, the geometric distortion is corrected using the method presented in Section 3.2, and the final circular image can be generated through image mosaicking. From the simulation results done so far, we are confident that the image formation algorithm is stable and effective for missile-borne circular-scanning SAR, even under highly maneuvering conditions. Our further study will focus on the impact of assuming the wrong calibration point height, and more precise geometric-distortion correction method by using an external DEM. Motion errors and factors which deteriorate the image quality will also be our further study.

Competing interests

The authors declare that they have no competing interests.

Acknowledgements

The authors wish to thank Dr. Daiyin Zhu from Nanjing University of Aeronautics and Astronautics for helpful technical discussions.

Received: 11 August 2012 Accepted: 7 December 2012

Published: 2 January 2013

References

1. WG Carrara, RM Majewski, RS Goodman, *Spotlight Synthetic Aperture Radar: Signal Processing Algorithms*, (Artech House, Norwood, 1995)
2. DE Wahl, PH Eichel, DC Ghiglia, PA Thompson, CV Jakowatz, *Spotlight-Mode Synthetic Aperture Radar: A Signal Processing Approach*. (Kluwer Academic Publishers, Boston, 1996)
3. IG Cumming, FH Wong, *Digital Processing of Synthetic Aperture Radar Data: Algorithms and Implementation*, (Artech House, Norwood, 2005)
4. B Deng, X Li, H Wang, Y Qin, J Wang, Fast raw-signal simulation of extended scenes for missile-borne SAR with constant acceleration. *IEEE Geosci. Rem. Sens. Lett.* **8**, 44–48 (2011)
5. B Sun, Y Zhou, T Li, J Chen, in *2006 International Conference on Radar*, vol. 1. Image formation algorithm for the implementation of circular scanning, SAR, (Shanghai, 2006), pp. 1–4
6. Y Li, D Zhu, The geometric-distortion correction algorithm for circular-scanning SAR imaging. *IEEE Geosci. Rem. Sens. Lett.* **7**, 376–380 (2010)
7. B Rigling, R Moses, Taylor expansion of the differential range for monostatic SAR. *IEEE Trans. Aerosp. Electron. Syst.* **41**, 60–64 (2005)
8. D Zhu, Z Zhu, Range resampling in the polar format algorithm for spotlight SAR image formation using the chirp z-Transform. *IEEE Trans. Signal Process.* **55**, 1011–1023 (2007)
9. D Zhu, Y Li, Z Zhu, A keystone transform without interpolation for SAR ground moving-target imaging. *IEEE Geosci. Rem. Sens. Lett.* **4**, 18–22 (2007)
10. G Fornaro, Trajectory deviations in airborne SAR: analysis and compensation. *IEEE Trans. Aerosp. Electron. Syst.* **35**, 997–1009 (1999)

doi:10.1186/1687-6180-2013-2

Cite this article as: Gao et al.: An image formation algorithm for missile-borne circular-scanning SAR. *EURASIP Journal on Advances in Signal Processing* 2013 **2013**:2.

Submit your manuscript to a SpringerOpen[®] journal and benefit from:

- Convenient online submission
- Rigorous peer review
- Immediate publication on acceptance
- Open access: articles freely available online
- High visibility within the field
- Retaining the copyright to your article

Submit your next manuscript at ► springeropen.com